# Compositionally graded organic-inorganic nanocomposites for enhanced thermoelectric performance

*Canlin Ou,[1] Lu Zhang,[1] Qingshen Jing,[1] Vijay Narayan[2] and Sohini Kar-Narayan[1]**

C. Ou, L. Zhang, Dr Q. Jing, Dr V Narayan Dr S. Kar-Narayan

[1]Department of Materials Science and Metallurgy, University of Cambridge, 27 Charles Babbage Road, Cambridge CB3 0FS, UK.

[2]Department of Physics, University of Cambridge, J. J. Thomson Avenue, Cambridge CB3 0HE, UK.

E-mail: sk568@cam.ac.uk

Keywords: thermoelectric, nanocomposites, aerosol-jet printing, thermal energy harvesting

Thermoelectric generators (TEGs) operate in the presence of a temperature gradient, where the constituent thermoelectric (TE) material converts heat into electricity via the Seebeck effect. However, TE materials are characterised by a thermoelectric figure of merit (*ZT*) and/or power factor (PF), which often has a strong dependence on temperature. Thus, a single TE material spanning a given temperature range is unlikely to have an optimal *ZT* or PF across the entire range, leading to inefficient TEG performance. Here, we demonstrate compositionally graded organic-inorganic nanocomposites, where the composition of the TE nanocomposite is systematically tuned along the length of the TEG, in order to optimise the PF along the applied temperature gradient. The nanocomposite composition can be dynamically tuned by an aerosol-jet printing method with controlled *in-situ* mixing capability, thus enabling the realisation of such compositionally graded thermoelectric composites (CG-TECs). We show how CG-TECs can be realised by varying the loading weight percentage of $Bi_2Te_3$ nanoparticles or $Sb_2Te_3$ nanoflakes within an organic conducting matrix using bespoke solution-processable inks. The enhanced energy harvesting capability of these CG-TECs from low-grade waste heat (<100 °C) is demonstrated, highlighting the improvement in output power over single-component TEGs.

## 1. Introduction

Harvesting energy from ambient sources in our environment such as light, thermal and vibrational sources has attracted increasing interest. Tapping into these alternative energy sources could potentially satisfy the high demand for self-powered, embedded, implantable, portable, wireless and/or wearable electronic devices that are presently powered by traditional batteries that need frequent recharging and/or replacing.[1–3] Harvesting thermal energy is particularly attractive as there are abundant environmental heat sources and most of them, such as the heat released by exhausts, industrial processes and radiators, or even that arising from human body heat, are mostly unexploited.[4] Thermoelectric generators (TEGs) based on thermoelectric (TE) materials are prime candidates for thermal energy harvesting due to their ability to convert ambient and ever-present waste heat into electrical energy by utilising the Seebeck effect.[5] TEGs have the potential to be scaled down in size and integrated into self-powered electronic devices with minimal maintenance.[6] However, a problem faced in this field is that existing inorganic TE materials often suffer from scarcity and/or toxicity. Furthermore, it is difficult to scale up the production of many of these materials, which are often not suitable for flexible and/or conformable applications due to their rigid nature. Accordingly, it is important for the future of this technology that new classes of TE materials are developed and evaluated. In order to evaluate the performance of TE materials, the dimensionless figure of merit (*ZT*) is usually used to describe their potential energy conversion efficiency. For a given operating temperature, *ZT* is defined as $ZT = S^2\sigma T / \kappa$, where $\kappa$ is the thermal conductivity [W/m.K], $\sigma$ is the electrical conductivity [S/m], and *S* is the Seebeck coefficient [V/K].[7,8] A good TE material therefore needs to possess a high *S* and $\sigma$ to ensure a high-voltage output at a given temperature difference. The power factor (PF= $S^2\sigma$) can also be used as an alternative way to evaluate TE materials, and increasing PF has been recognised as a key strategy in optimising *ZT*,[8] particularly in the case of polymer-based TE materials where $\kappa$ values are

relatively low and similar in magnitude. TE materials with a higher PF value can convert more heat into electricity.

One of the most pressing issues that researchers in this field are facing is the development of high-performance TE materials, which has proven to be difficult. Binary bulk chalcogenides such as bismuth telluride ($Bi_2Te_3$) and antimony telluride ($Sb_2Te_3$) are well-known to exhibit a maximum *ZT* value of more than 1.4 at room temperature, and are thus well-suited for near-room-temperature applications, such as refrigeration and waste heat recovery up to 200 °C.[10–12] However, using expensive inorganic TE modules to harvest thermal energy is largely impractical. Hence, all these factors have drawn significant interest in developing efficient, scalable, inexpensive, and flexible TE devices. Although organic TE materials are currently unable to match the performance of their inorganic counterparts, they can be inexpensive, scalable, and mechanically flexible alternatives for some applications, such as those aimed at human body integration, or waste heat recovery from hot water pipes, where there is a requirement to be lightweight and flexible/conformal.[7] Among the recently reported TE polymers, *p*-type poly(3,4-ethylenedioxythiophene) polystyrene sulfonate (PEDOT:PSS) has been shown to possess one of the highest TE performance capabilities at low cost, ease of large-volume and/or large-area printed organic electronic manufacturing, and excellent environmental stability.[2,12,13] Therefore, PEDOT:PSS has been selected as the organic polymer matrix in this work, as it can be readily processed with very low intrinsic $\kappa$.[14] Additionally, nanocomposite structuring methods can also be an effective approach to split the interdependence of electrical charge carriers and thermal carriers (electrons and phonons, respectively), thus significantly reducing $\kappa$ without adversely affecting *S* and $\sigma$ via selective phonon scattering at interfaces, thereby leading to greater *ZT* as a whole.[15–18]

Numerous studies have been conducted on the enhancement of single-phase TE materials, with relatively fewer studies on the development of organic-inorganic hybrids, which have been

shown to overcome some of the difficulties associated with single-phase materials.[2,14,20–23] Nevertheless, all TE materials suffer from a problem that their *ZT* or PF values often have a strong dependence on temperature. Accordingly, even where it is possible to provide alternative TE materials which overcome some known problems of traditional TE materials, there is still the issue that TE materials can only ever be efficient within a small temperature range due to the variation of PF with temperature. This leads to a more serious and often overlooked issue, particularly when using a homogeneous single-phase TE material over a wide temperature range, without considering the position-dependent *ZT* and/or PF, thus leading to inefficient thermal-to-electrical energy conversion. This problem was first considered in the context of inorganic TE materials in work by Ioffe *et al*.,[23] where the concept of functionally graded thermoelectric material (FG-TEM) design was proposed, that could lead to 50 - 100 % improvement in device efficiency with the use of existing inorganic TE materials.[14,24–26] FG-TEMs are inhomogeneous materials with a spatial gradation in the composition and/or structure of materials, resulting in a corresponding variation in their thermoelectric, electrical, thermal, and/or mechanical properties.[14,27] As reported in the literature, FG-TEMs can be designed as continuous-graded structures or segmented-graded structures, depending on the material characteristics, processing methods, and/or their applications. The key challenge is to replace the sharp interfaces within the traditional composite structure with graded interfaces that may be achieved by tuning chemical composition, microstructure or porosity. For 'continuous FG-TEMs', as they are generally referred to in the literature, a single-phase inorganic TE material is modified to provide different carrier concentrations in different regions of the material. Although no additional interface is introduced between the different regions, it has proven to be difficult to fully optimise the *ZT* values within the temperature ranges studied, as it has been challenging to control diffusion of carriers through the material, in particular when used at elevated temperatures, which can cause deterioration of device performance and lifetime.[25,26,28–40] Furthermore, the current research on continuous FG-TEMs is still at the

proof-of-concept stage, and it is not clear that the grading in these materials can be well controlled during mass-manufacturing processes. On the other hand, 'segmented FG-TEMs' have been developed to comprise multiple dissimilar segments having different TE properties into one whole TE element, where the optimum performance of individual component can be fully utilised without compromising over large temperature ranges.[10,35,41–50] This design has been the most commonly used in the literature as it can be easily fabricated with materials having optimum *ZT* values at different applied temperatures, for instance in the case where SiGe was used for high-temperature range, PbTe for medium temperature range, and $Bi_2Te_3$ for low-temperature range.[24–26] However, one significant drawback of such an approach is the difficulty of connecting multiple dissimilar materials without the introduction of interfaces that are prone to failure due to the thermo-mechanical stress at such interfaces in the presence of different thermal expansion coefficients during practical use. The introduction of such physical interfaces also lowers the overall electrical conductivity, which has a negative impact on TE performance. Additionally, elemental diffusion and contamination, especially at high temperatures, could also deteriorate the device performance and lifetime.[14,24–26,35]

Most of the research into graded TEGs has been done by solely using conventional single-phase inorganic TE materials to verify the FG-TEM concept, and there is currently no report on adopting this concept for polymeric and/or composite TE materials, which could serve as a way to boost TE performance of hybrid TE materials and devices. Conventional TEGs comprise several vertically aligned 3-D bulk legs electrically connected in series by metallic contacts and thermally connected in parallel between two ceramic substrates, where the vertical heat flow is along the TE legs. However, since most organic and/or solution-processed inorganic materials do not benefit from such geometrical configuration, in this work, a 2-D device architecture with a lateral heat flow is purposed to exploit the possibility of printing flexible thermoelectrics.[51] Thus, the aim and objective of this work is to develop "compositionally" graded nanocomposite

TEGs, suitable for harvesting energy from the low-grade waste heat (<100°C), where the PF is optimised to work effectively over the whole temperature range by varying the composition of the organic-inorganic nanocomposite, by appropriately tuning the loading fraction of the inorganic nano-filler in a conducting polymeric matrix, along the length of the TEG. The impact on the TE properties of printed PEDOT:PSS-based TE nanocomposites with various loading weight percentage of $Bi_2Te_3$ nanoparticles and $Sb_2Te_3$ nanoflakes has been well investigated in our previously published work,[2,13] showing improvement of PF values for certain compositions. Here, a compositionally graded thermoelectric composite (CG-TEC) structure is adopted to enhance the overall thermal-to-electrical conversion efficiency of a fully printed TEG. We show that the CG-TEC structure can be fabricated by using two separate ink sources (one organic, and the other inorganic), which can be mixed *in-situ* using an aerosol jet printing (AJP) technique.[2,13] The AJP atomises functional inks into an aerosol droplet form. The aerosol droplets are subsequently streamed through a deposition head and focused by a nitrogen gas flow (i.e. sheath flow) before deposition onto a substrate to form the TE nanocomposite.[2,13] Several significant benefits of the AJP technique compared to other printing techniques have been widely reported in the literature.[2,52] In this work, the AJP technique is used to dynamically tune the composition of a printed nanocomposite to realise the CG-TEC structure with an optimised composition variation to match the temperature gradient across which the printed CG-TEC operates during use.

## 2. Results and Discussion

### 2.1. Temperature-dependent Power Factor of Printed Nanocomposites

Since both $S$ and $\sigma$ are temperature-dependent TE properties, the PF also has a temperature dependence, i.e. PF($T$). In order to obtain the highest power output and/or overall efficiency of the TEG, appropriate material composition should be selected locally to achieve a desired PF

response across the entire temperature range of use of the TE material. To achieve this, different printed PEDOT:PSS-based TE nanocomposites were prepared and measured to investigate how different loading ratios of inorganic components contribute to the temperature-dependent TE properties, via a custom-built measurement setup as described in detail in the Experimental Section and Supporting Information S1 and S2. The graphs of PF vs temperature of different printed PEDOT:PSS-based nanocomposites loaded with different wt.% of various nanomaterials were plotted and compared in Figure 1a. It can be seen that each of the TE nanocomposites investigated here displayed a different PF response with temperature. The TE data for each sample is plotted and compared in Supporting Information S3. In order to prove the CG-TEC concept, three specific compositions were selected for a closer view and plotted as shown in Figure 1b, to find out the appropriate combination of materials compositions that would optimise TE performance over the temperature range of interest. The intention was to pair up compositions such that one had a higher PF at the lower temperature range while the other had a higher PF at the higher temperature range, when compared to each other, i.e. compositions with a "crossover" of PFs across the entire temperature range. Therefore, by appropriately tuning the composition across the whole range, an overall enhanced thermoelectric performance could be achieved than when using either single composition across the whole temperature range.

To start with, a pristine PEDOT:PSS sample was prepared, and a temperature-dependent TE measurement was conducted, as shown in Figure S3. It can be seen that the *S* values increased in direct proportion to the sample temperature and yielded the highest value of ~26.8 μV/K at 363 K. The $\sigma$ increased with increasing temperature, peaking at 343 K with a value of 704.5 S/cm. However, with further increase in temperature, the $\sigma$ decreased slightly. As a combination of the increased *S* and $\sigma$, the maximum PF value of ~50.2 μW/mK$^2$ was recorded at 363 K. For a doped semiconductor, its $\sigma$ value generally increases steeply with the

temperature at the low range of temperature due to the loss of carriers from the donors or acceptors, following which the $\sigma$ value starts decreasing slightly due to reduced mobility of carriers.[53] Since the PEDOT:PSS polymer used here is a doped semiconductor, our measured results followed a similar $\sigma$ response profile with temperature. Following this, $Bi_2Te_3$-PEDOT:PSS nanocomposite samples loaded with 15 wt.%, 35 wt.%, 50 wt.%, 65 wt.%, 85 wt.% and 90 wt.% $Bi_2Te_3$ nanoparticles were printed and measured over the temperature range of 293K to 363K. The TE data for each composition has been separately plotted in Figure S4. From the different temperature-dependent TE profiles of these $Bi_2Te_3$-PEDOT:PSS nanocomposites, it can be seen that with increased loading of the inorganic components, the *S* values increased more dramatically, while the $\sigma$ values dropped even more steeply with increasing temperature, resulting in a gradually increasing PF response with temperature, all peaking at 363 K. These data indicate that adding metallic components rendered the nanocomposite more metal-like, as expected. As the number of free electrons in a unit volume of the conductor or semiconductor rises exponentially with increasing temperature, this leads to the dramatic decline in the relaxation time as well as the mean free path, and thereby a significant drop in the $\sigma$ values.[53] With the increasing amount of loaded $Bi_2Te_3$ nanoparticles, this phenomenon became more distinct. Finally, the temperature-dependent TE properties of $Sb_2Te_3$-PEDOT:PSS nanocomposite samples loaded with 15 wt.%, 35 wt.%, 50 wt.%, 65 wt.%, 85 wt.%, and 90 wt.% of $Sb_2Te_3$ nanoflakes were plotted and compared in Figure S5. In this group, it shows that the $\sigma$ values decreased with the increase of temperature, which indicates more metal-like behaviour of the nanocomposites. The significant enhancement in *S* led to all the PF values of different printed nanocomposites peaking at 363 K, which might be attributed to the higher *S* value of the *p*-type $Sb_2Te_3$ nanoflakes. Note that printed structures comprising only inorganic nanoparticles without the conducting polymer matrix were found to be electrically non-conducting.[2]

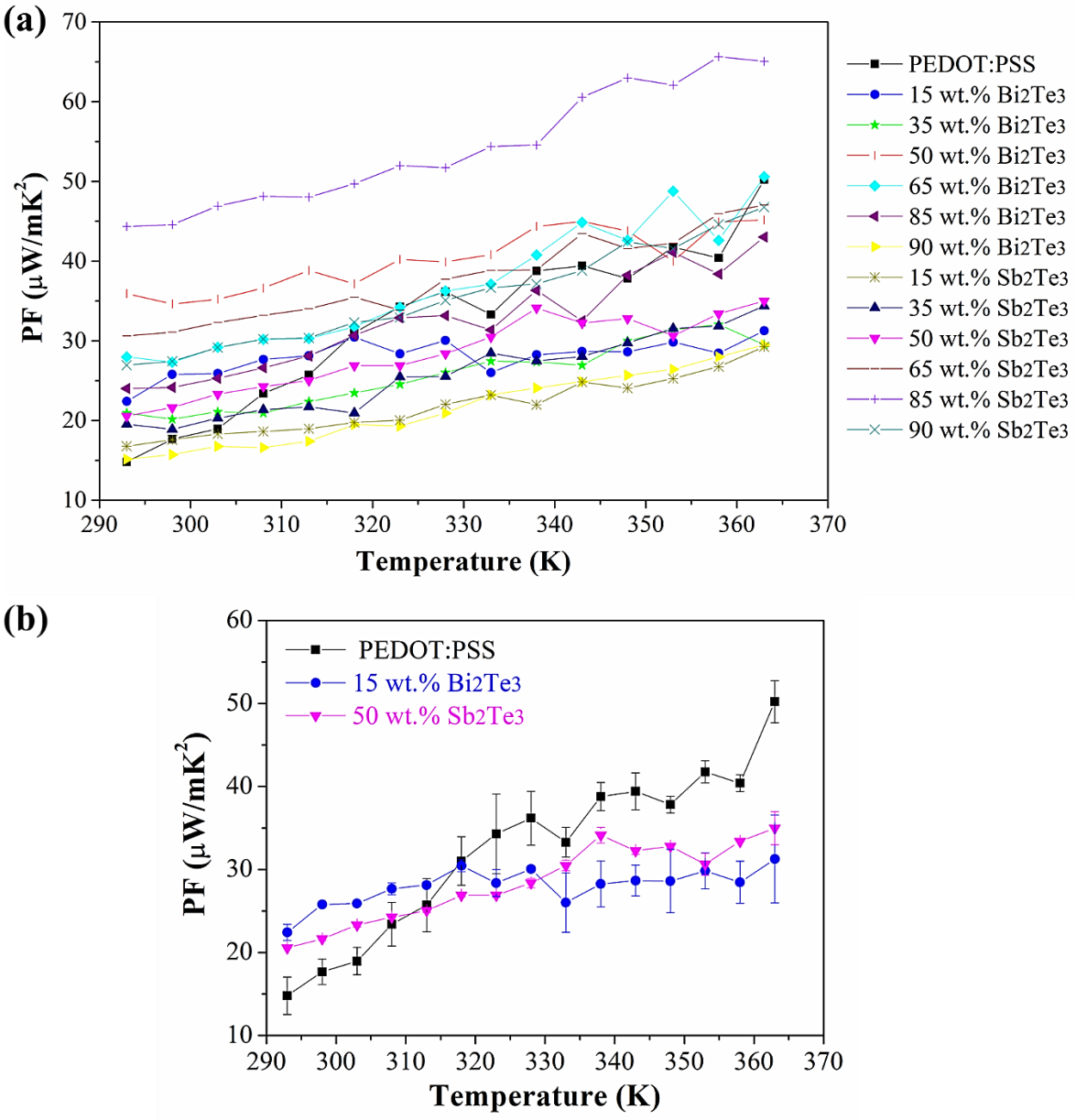


**Figure 1.** (a) Temperature-dependent PF measurements of printed PEDOT:PSS-based nanocomposites loaded with different wt.% of various nanomaterials (not compositionally graded). (b) Closer view of 3 specific compositions for subsequent composition optimisation in the CG-TEC structure design.

### 2.2. Compositionally Graded Thermoelectric Composites (CG-TECs)

The temperature-dependent PF values of different pairs of printed TE materials are shown below in Figure 2, spanning the temperature range of interest. It can be seen in Figure 2a that the PF values of 15 wt.% $Bi_2Te_3$-PEDOT:PSS nanocomposite and pristine PEDOT:PSS intersect at a temperature $T_x$ of 318 K. The 15 wt.% $Bi_2Te_3$-PEDOT:PSS nanocomposite exhibited higher PF values than that of pristine PEDOT:PSS below 318 K, while above that, the pristine PEDOT:PSS surpassed the nanocomposite. Similarly, Figure 2b shows the PF values of 50 wt.% $Sb_2Te_3$-PEDOT:PSS nanocomposite and pristine PEDOT:PSS, where the intersection temperature $T_x$ was 313 K. The solid green lines on Figure 2 indicate the highest PF that could be obtained through a combination of the respective compositions above and below $T_x$. Therefore, using these graphs, a compositionally graded thermoelectric composite (CG-TEC) could be designed and fabricated, where different material compositions are realised to work across different temperature ranges, according to whichever correspondingly exhibits the higher PF.

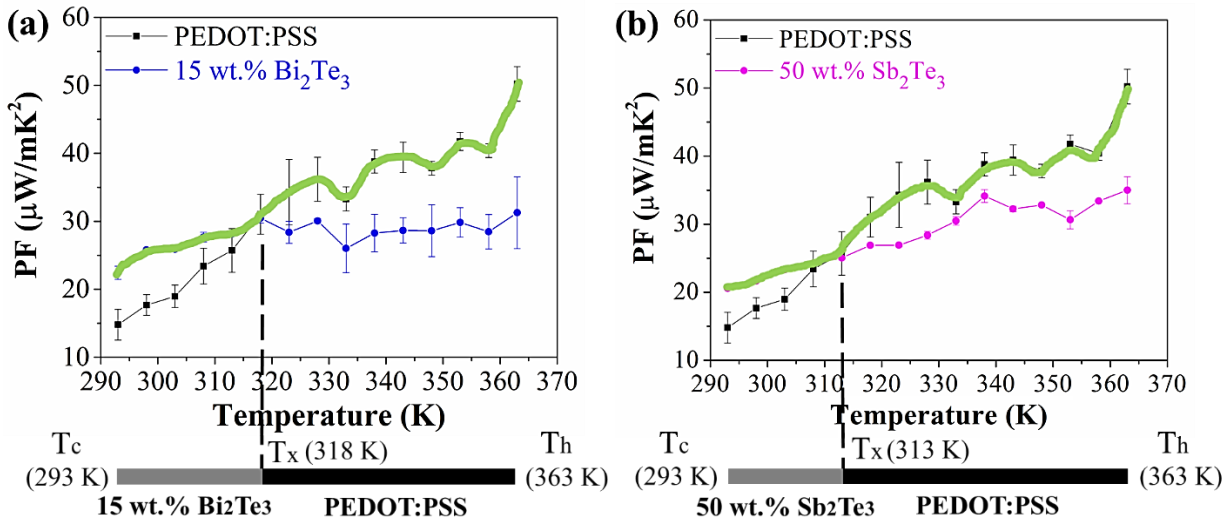


**Figure 2.** Temperature-dependent measurements of PF for (a) 15 wt.% $Bi_2Te_3$-PEDOT:PSS nanocomposite and PEDOT:PSS, and (b) 50 wt.% $Sb_2Te_3$-PEDOT:PSS nanocomposite and PEDOT:PSS, respectively, indicating a crossover temperature where one composition

outperforms the other.

In the examples discussed below, the boundary between the first and second portions was selected to be at or near the location of the intersection temperature of the PF response profiles of the two materials, as calculated by modelling the theoretical temperature distribution along the length of TEG operating under a given temperature gradient. To design the printing pattern for the CG-TEC sample, a finite element analysis (FEA) simulation using COMSOL Multiphysics (see Figures 3 a & b) was conducted to simulate the heat flow and temperature distribution along with the CG-TEC samples, where the black line indicates the location of $T_x$, which accordingly defines the boundary between the first and second components. The temperature at either end was set to 293 K and 363 K respectively to provide a 70 K temperature difference across the whole TEG. The effect of contact thermal resistance at the interface was neglected as the same polymer matrix was used across the interface, and the volumetric loading fraction of the nanoparticles was low. This also led to a relatively small variation in thermal conductivity across the interface . It should be noted that the calculation and prediction of the thermal conductivity of polymer-based composites is highly complicated as it is a function of the filler structure and its dispersion, intrinsic thermal conductivity of both the filler and polymer, as well as interfacial thermal resistance.[54] Nevertheless, the effective thermal conductivity of the composite can be calculated using Maxwell's formula,[55–57] as shown in Supporting Information S4, where the phonon scattering at the organic-inorganic interface is not considered. This gives an upper bound for thermal conductivity of the composite, which is found to be only slightly higher than the pristine polymer matrix, due to the low loading volume fractions (see Figure S6). The resultant thermal conductivity of our polymer-based composites would be further reduced due to the phonon scattering effect as explained in the literature,[9,15,17] which is advantageous from the point of view of thermoelectric performance.

According to the above temperature-dependent measurement results, the boundary temperature that was used for the CG-TEC design was located by varying the length of different components under the simulated temperature distribution, as discussed in detail in Supporting Information S5. For the CG-TEC comprising 15 wt.% $Bi_2Te_3$-PEDOT:PSS nanocomposite + PEDOT:PSS, the boundary location was determined to be approximately 7.5 mm from the cold end of a 20 mm long TEG (i.e. 0 mm to 7.5 mm was composed of 15 wt.% $Bi_2Te_3$-PEDOT:PSS nanocomposite, while 7.5 mm to 20 mm was pristine PEDOT:PSS). For the CG-TEC comprising 50 wt.% $Sb_2Te_3$–PEDOT:PSS + PEDOT:PSS, the boundary location was approximately 8 mm from the cold end. As illustrated in Figures 3 c & d, the AutoCAD-designed patterns were derived accordingly, and the CG-TEC samples were printed by an AJP technique, as discussed in the Experimental Section. It should be noted that the individual components in these AJ-printed CG-TEC samples were connected without using additional electrical joints, thus avoiding the creation of interfaces and/or defects within the TEG. Additionally, single-phase pristine PEDOT:PSS, 15 wt.% $Bi_2Te_3$-loaded nanocomposite, and

50 wt.% $Sb_2Te_3$-loaded nanocomposite were also prepared as control samples to compare their TE performance with that of CG-TEC samples.

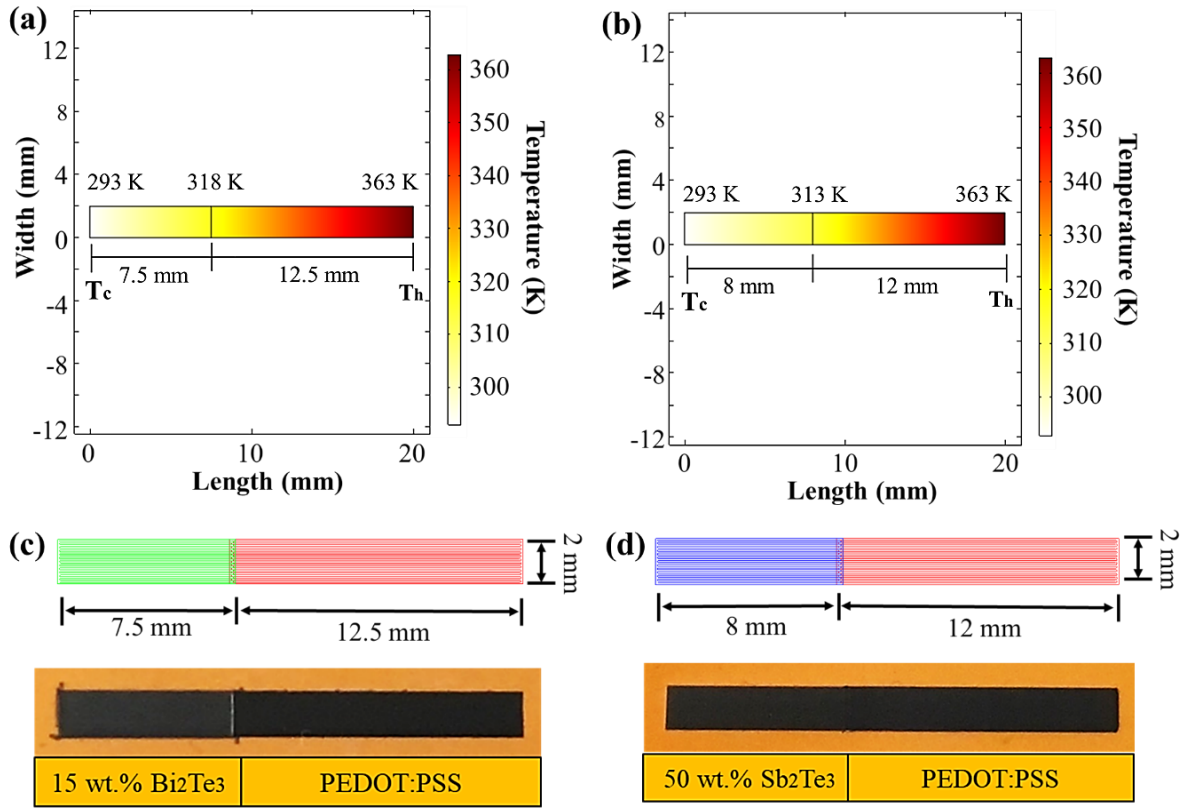


**Figure 3.** COMSOL simulation results showing the temperature distribution profile along with the sample of (a) 15 wt.% $Bi_2Te_3$-PEDOT:PSS nanocomposite + PEDOT:PSS CG-TEC and (b) 50 wt.% $Sb_2Te_3$-PEDOT:PSS nanocomposite + PEDOT:PSS CG-TEC, respectively. Diagram of the compositionally graded structure of the AutoCAD-designed pattern and the experimentally printed sample of (c) CG-TEC comprising 15 wt.% $Bi_2Te_3$-PEDOT:PSS nanocomposite + PEDOT:PSS, and (d) CG-TEC comprising 50 wt.% $Sb_2Te_3$-PEDOT:PSS nanocomposite + PEDOT:PSS, respectively.

Figure 4 shows the interface between the two printed components was quite smooth and uniform. Since the PEDOT:PSS polymeric matrix is the same across the whole length, the 15 wt.% $Bi_2Te_3$-PEDOT:PSS nanocomposite phase and pure PEDOT:PSS phase were well mixed

in the transition region, thereby providing a variation of composition over a narrow region across the interface, as seen in the surface morphology. In other words, there was no step-change in composition between the two components of the CG-TEC. This smoothly graded interface serves to avoid otherwise common interface problems, e.g. cracks and other defects introduced and accumulated due thermal misfit and thermo-mechanical stress, and in particular, due to diffusion or contamination issues arising at the joints of dissimilar components, which could otherwise significantly degrade the performance and lifetime of the TEG.

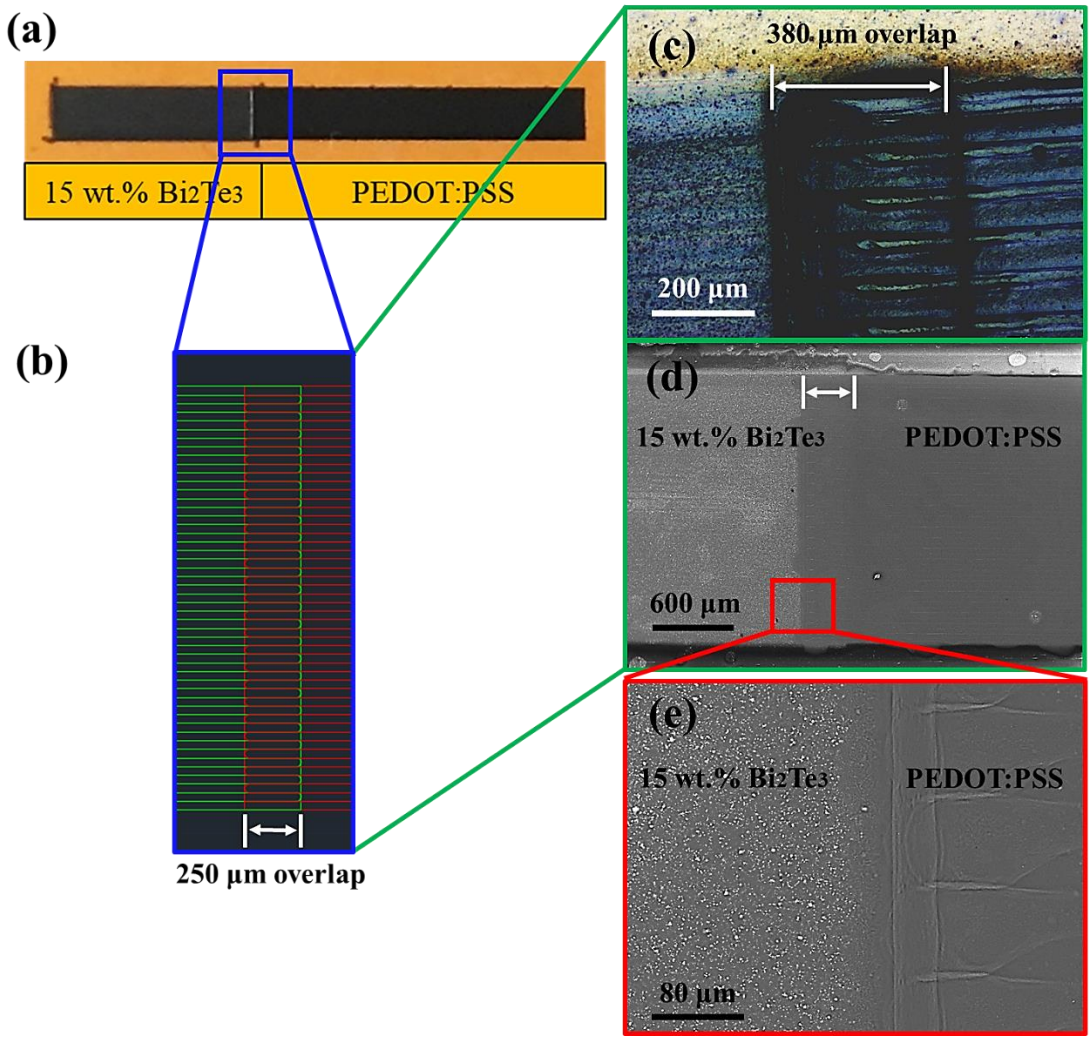


**Figure 4.** (a) Photo of a printed 15 wt.% $Bi_2Te_3$-PEDOT:PSS nanocomposite + PEDOT:PSS CG-TEC. (b) Enlarged AutoCAD-designed pattern showing the overlap part between two different designed components. (c) Optical microscope image and (d) scanning electron

microscope (SEM) image of the transition region between the two different components of the CG-TEC, where more details of the interface are revealed in (e) the enlarged SEM image.

### 2.3. Compositionally Graded Thermoelectric Generators (CG-TEGs)

A custom-designed measurement setup, as shown in Figure S11, was used for measuring the voltage generated by samples with a constant $\Delta T$ applied along the lateral direction. The compositionally graded thermoelectric generators (CG-TEGs) were designed, assembled, and tested under variable load resistances to determine their maximum power output at impedance-matched conditions, as discussed in the Experimental Section and Supporting Information S6. These printed TEGs can be viewed as thermal batteries, where the electromotive force is the Seebeck voltage $\Delta V = - S \Delta T$. The maximum power output was determined via the impedance matching across variable load resistors under a constant applied temperature difference $\Delta T$ ~70 K. The external load resistance ($R_L$) was varied from 1 Ω to 1 MΩ via a resistance decade box, and the output voltage across them was measured via a Keithley 2002 digital multimeter, where the output power $P = V^2 / R$ was calculated accordingly. The maximum output power was achieved when the internal sample resistance ($R_S$) equalled the external load resistance, i.e. $R_S = R_L$. Figure 5 shows the voltage output and power output plotted as a function of $R_L$ for single-phase TEGs as well as CG-TEGs under the same $\Delta T$ of 70 K. Our results clearly show that for the same $\Delta T$, the CG-TEGs outperformed the single-phase TEGs.

In order to verify the CG-TEG concept, the power outputs of the CG-TEGs were tested in two configurations: first, the temperature gradient was applied along the correct direction (i.e. 15 wt.% $Bi_2Te_3$-loaded nanocomposite and 50 wt.% $Sb_2Te_3$-loaded nanocomposite part on the "cold" side, respectively, and PEDOT:PSS on the "hot" side, as referred to as "good design" in Supporting Information S5), and second, the temperature gradient was reversed, such that the

respective PFs were not the highest in the correct temperature ranges ("bad design" as described in Figure S9 and Figure S10). In the case of the single-phase printed TEGs, there was no significant difference in their output power when switching the temperature gradient direction, as expected. However, a decrease in the output power was seen in both CG-TEGs when the temperature gradient was applied in the reverse direction, as shown in Figure S12, which indicated that these CG-TEGs were not utilised in their optimum operating condition. It can be seen in Figure S13 that the output power of both CG-TEGs with "bad design" was significantly decreased by more than half, leading to the values that were even lower than their single-phase counterparts. Therefore, proper material matching as well as device design are of utmost importance to maximise the output power of these CG-TEGs.

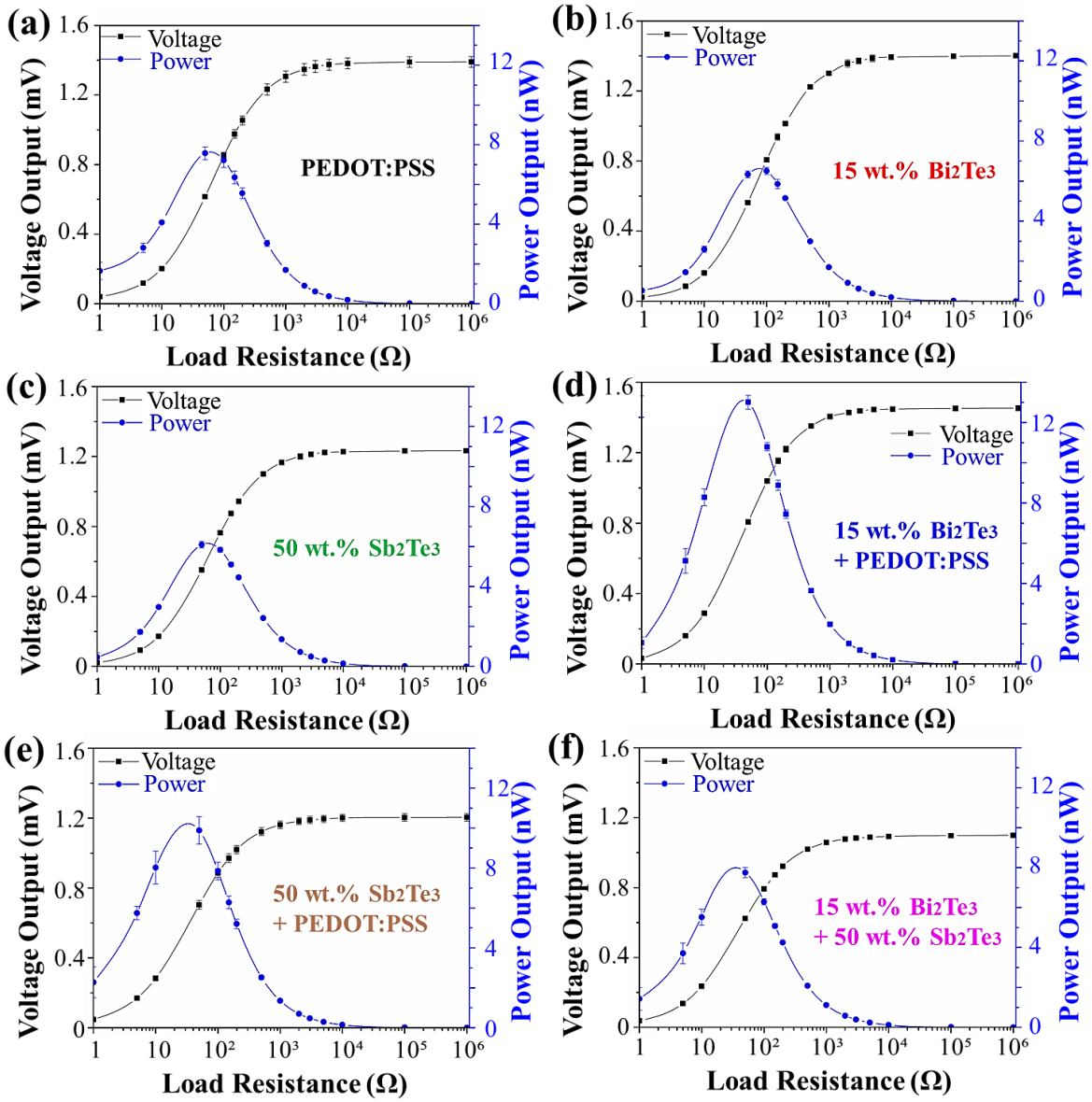


**Figure 5.** The output voltage and output power against various external load resistance of (a) pristine PEDOT:PSS film (not compositionally graded), (b) 15 wt.% $Bi_2Te_3$-PEDOT:PSS nanocomposite (not compositionally graded), (c) 50 wt.% $Sb_2Te_3$-PEDOT:PSSnanocomposite (not compositionally graded), (d) CG-TEG comprising 15 wt.% $Bi_2Te_3$-PEDOT:PSS nanocomposite + PEDOT:PSS, (e) CG-TEG comprising 50 wt.% $Sb_2Te_3$-PEDOT:PSS nanocomposite + PEDOT:PSS CG-TEG, and (f) CG-TEG comprising 15 wt.% $Bi_2Te_3$-PEDOT:PSS nanocomposite + 50 wt.% $Sb_2Te_3$-PEDOT:PSS nanocomposite, respectively, under a same temperature difference of 70 K.

It was found that all the TEGs tested exhibited maximum power output across an external load resistance of 50 Ω. For a more straightforward comparison of the power output between different samples, all the power output values at 50 Ω were re-plotted as shown in Figure 6. It is evident that each of the CG-TEGs were superior to their non-compositionally-graded (single-phase) counterparts under the same applied temperature difference. Among them, the 15 wt.% CG-TEG comprising $Bi_2Te_3$-PEDOT:PSS nanocomposite + PEDOT:PSS exhibited the most enhanced power output value ~13 nW and power area density of ~100 μW/cm$^3$, and the CG-TEG comprising 50 wt.% $Sb_2Te_3$-PEDOT:PSS nanocomposite + PEDOT:PSS came second with a power output of ~10 nW. Our studies show that the CG-TEG design is particularly effective in enhancing TE performance and power output compared with non-compositionally graded homogeneous TEGs.

Since only a single TE leg was used in each TEG for ease of comparison between the different samples, only a relatively small difference in power output was seen. However, this difference could be amplified by the use of a plurality of such TE legs in a practical TEG device. In order to further investigate the practical application of these printed CG-TEGs, 20 TE legs comprising 15 wt.% $Bi_2Te_3$-PEDOT:PSS nanocomposite + PEDOT:PSS CG-TECs, were AJ-printed onto a flexible polyimide sheet (see Figure S14), and they were connected to each other electrically in series and thermally in parallel by silver electrodes. An open-circuit voltage $V_{oc}$ ~12.5 mV, short-circuit current $I_{sc}$ ~11.3 μA, and maximum power $P_{max}$ ~141 nW was generated from this CG-TEG under the operating temperature difference $\Delta T$ ~ 50 °C, with an internal electrical resistance $R_{int}$ ~954 Ω. It proves that this CG-TEG can be used for thermal energy harvesting in a wearable device, or for waste heat recovery e.g. from hot water pipes up to 100 °C.

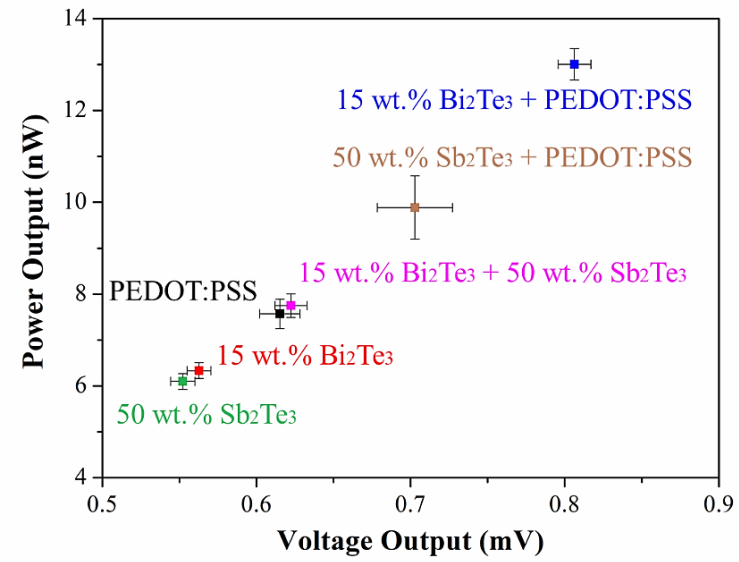


**Figure 6.** The comparison of output voltage and output power of 6 different aerosol-jet printed thermoelectric samples under the same applied temperature gradient across an external load resistance of 50 Ω under a temperature difference of 70 K.

## 3. Conclusion

In this work, we explored the temperature-dependent thermoelectric properties of aerosol-jet printed PEDOT:PSS-based nanocomposites loaded with various $Bi_2Te_3$ nanoparticles and $Sb_2Te_3$ nanoflakes. By selecting the proper compositions based on the temperature-dependent PF profiles, compositionally graded thermoelectric generators (CG-TEGs) were designed, and their power output values were found to be higher than non-compositionally graded counterparts. This shows that our CG-TEG design provides a means by which the thermoelectric performance and efficiency of organic-inorganic nanocomposite-based TEGs can be enhanced, and therefore opens the door to wide range of combinations comprising a variety of different conducting polymers and inorganic nano-fillers that could be tailored for use across specific temperature gradients.

## 4. Experimental Section

*Ink formulation:* The poly(3,4-ethylenedioxythiophene) polystyrene sulfonate (PEDOT:PSS, 1 wt.%, Heraeus Clevious™ PH1000) used in this project was purchased from Ossila. The $Bi_2Te_3$ nanoparticles and $Sb_2Te_3$ nanoflakes were synthesised by a scalable solvothermal synthesis process, and both of their conducting behaviour is *p*-type[2]

*Aerosol jet printing (AJP):* Before the printing process, a printing pattern was designed and drawn using the AutoCAD software as illustrated in Figure S1a. Then, the aerosol-jet printer (Optomec Aerosol Jet 200 Printer) equipped with an ultrasonic atomiser (UA) and a pneumatic atomiser (PA) was used here to print $Bi_2Te_3$ or $Sb_2Te_3$ nanocrystals with a combination of PEDOT:PSS as matrix onto a flexible polyimide substrate (PI, 75 μm thick, Goodfellow®). After printing, the printed samples were cured at 130 °C for 30 min to remove water and other undesirable organic solvents as obtained in Figure S1b. Moreover, 5 wt.% of ethylene glycol (EG, 99.8%, Sigma-Aldrich) was added into the PEDOT:PPS ink, and a post-curing surface treatment was also conducted to improve the final Seebeck coefficient and electrical conductivity of PEDOT:PSS matrix as we previously reported.[2,13] Various loading weight percentage (wt.%) of solvothermal-synthesised $Bi_2Te_3$ and $Sb_2Te_3$ nanocrystals (from 0 to 100 wt.% in nominal) were incorporated into the PEDOT:PSS matrix. This allowed us to analyse how the loading inclusions contribute to the TE properties of the printed PEDOT:PSS-based TE nanocomposites with the dependence of temperature.

*Dimension measurement:* Following the sample printing, the length and width of printed strips were measured by a table-top scanning electron microscope (Hitachi TM3000) or by an optical microscope (Nikon Optiphot), whilst their thickness was measured by a stylus profilometer (Veeco DEKTAK). The thickness values of all the aerosol-jet printed TE films range from 1 to 1.5 μm. For each sample, a minimum of three repeated measurements were

conducted, with the average value being calculated to increase the accuracy. Given the measured dimensions, the electrical conductivity of a printed strip was then calculated by knowing its resistance value via the four-point probe measurement.

*Temperature-dependent Thermoelectric Measurement:* Different PEDOT:PSS-based nanocomposites loaded with different ratio of inorganic components were prepared and measured via an in-house designed measurement setup as discussed in the Supporting Information S2. The $S$ and $\sigma$ values of each material composition sample were measured with the dependence of temperature ranging from 293K to 363K varied by the hot plate and/or the water-cooling system. The error bars were calculated from the measured values of two repeated measurements for the same loading ratio sample.

*Compositionally Graded Thermoelectric Generator Fabrication and Measurement:* For the fabrication of printed CG-TEGs, the aerosol flow rates from the different atomisers in fluid connection with respective different ink sources were adjusted during the printing process to dynamically tune the composition of the material being printed, thereby varying the loading wt.% of the $Bi_2Te_3$ and $Sb_2Te_3$ nanocrystals within the PEDOT:PSS matrix along the length of the printed composite material.[2,13] Then, a home-built setup, as shown in Figure S11, was designed to determine the maximum power output of these printed CG-TEGs by connecting with various external loaded resistors via a resistance decade box. In order to control a precise temperature different between either end of the thermoelectric leg, two Pt-100 thermocouples were attached next to their edges so that the real-time temperature was known and could be adjusted accordingly via two Peltier module controllers, where one was performed as a heat source while the other as a heat sink to ensure a stable temperature gradient over the sample.

**Supporting Information**
Supporting Information is available from the Wiley Online Library or from the author.

**Acknowledgements**
This work was financially supported by a grant from the European Research Council through an ERC Starting Grant (Grant no. ERC–2014–STG–639526, NANOGEN). S.K-N acknowledges support from the EPSRC grant "Centre for Advanced Materials for Integrated Energy Systems (CAM-IES)" EP/P007767/1. C.O. thanks the Cambridge Trust and China Scholarship Council for studentship support.

Received: ((will be filled in by the editorial staff))
Revised: ((will be filled in by the editorial staff))
Published online: ((will be filled in by the editorial staff))

## References

[1] M. Martín-González, O. Caballero-Calero, P. Díaz-Chao, *Renew. Sustain. Energy Rev.* **2013**, *24*, 288.

[2] C. Ou, A. L. Sangle, A. Datta, Q. Jing, T. Busolo, T. Chalklen, V. Narayan, S. Kar-Narayan, *ACS Appl. Mater. Interfaces* **2018**, *10*, 19580.

[3] C. Ou, P. E. Sanchez-Jimenez, A. Datta, F. L. Boughey, R. A. Whiter, S.-L. Sahonta, S. Kar-Narayan, *ACS Appl. Mater. Interfaces* **2016**, *8*, 13678.

[4] C. B. Vining, *Nat. Mater.* **2009**, *8*, 83.

[5] P. J. Taroni, I. Hoces, N. Stingelin, M. Heeney, E. Bilotti, *Isr. J. Chem.* **2014**, *54*, 534.

[6] Y. Chen, Y. Zhao, Z. Liang, *Energy Environ. Sci.* **2015**, *8*, 401.

[7] B. Russ, A. Glaudell, J. J. Urban, M. L. Chabinyc, R. A. Segalman, *Nat. Rev. Mater.* **2016**, *1*, 16050.

[8] T. M. Tritt, M. a Subramanian, *MRS Bull.* **2006**, *31*, 188.

[9] B. Poudel, Q. Hao, Y. Ma, Y. Lan, A. Minnich, B. Yu, X. Yan, D. Wang, A. Muto, D.

Vashaee, X. Chen, J. Liu, M. S. Dresselhaus, G. Chen, Z. Ren, *Science* **2008**, *320*, 634.

[10] G. J. Snyder, E. S. Toberer, *Nat. Mater.* **2008**, *7*, 105.

[11] R. Venkatasubramanian, E. Siivola, T. Colpitts, B. O'Quinn, *Nature* **2001**, *413*, 597.

[12] O. Bubnova, Z. U. Khan, A. Malti, S. Braun, M. Fahlman, M. Berggren, X. Crispin, *Nat. Mater.* **2011**, *10*, 429.

[13] C. Ou, A. L. Sangle, T. Chalklen, Q. Jing, V. Narayan, S. Kar-Narayan, *APL Mater.* **2018**, *6*, 096101.

[14] C. L. Cramer, H. Wang, K. Ma, *J. Electron. Mater.* **2018**, *47*, 5122.

[15] B. Zhang, J. Sun, H. E. Katz, F. Fang, R. L. Opila, *ACS Appl. Mater. Interfaces* **2010**, *2*, 3170.

[16] Y. Chen, M. He, B. Liu, G. C. Bazan, J. Zhou, Z. Liang, *Adv. Mater.* **2017**, *29*, 1604752.

[17] M. S. Dresselhaus, G. Chen, M. Y. Tang, R. G. Yang, H. Lee, D. Z. Wang, Z. F. Ren, J.-P. Fleurial, P. Gogna, *Adv. Mater.* **2007**, *19*, 1043.

[18] Y. Zhang, Y.-J. Heo, M. Park, S.-J. Park, *Polymers (Basel).* **2019**, *11*, 167.

[19] M. He, F. Qiu, Z. Lin, *Energy Environ. Sci.* **2013**, *6*, 1352.

[20] Q. Zhang, Y. Sun, W. Xu, D. Zhu, *Adv. Mater.* **2014**, *26*, 6829.

[21] M. Culebras, C. Gómez, A. Cantarero, *Materials (Basel).* **2014**, *7*, 6701.

[22] A. Shakouri, *Annu. Rev. Mater. Res.* **2011**, *41*, 399.

[23] A. F. Ioffe, Byulleten' Izobretenii **1960**, 126158.

[24] E. Müller, Č. Drašar, J. Schilz, W. A. Kaysser, *Mater. Sci. Eng. A* **2003**, *362*, 17.

[25] I. Shiota, A. Nishida, *16th Int. Conf. Thermoelectr.* **1997**, 364.

[26] J. Teraki, T. Hirano, *4th Int. Symp. Funct. Graded Mater.* **1997**, 483.

[27] C. C. Ge, X. F. Wu, G. Y. Xu, *Key Eng. Mater.* **2007**, *336–338*, 2600.

[28] L. I. Anatychuk, L. N. Vikhor, *16th Int. Conf. Thermoelectr.* **1997**, 588.

[29] O. Meroz, Y. Gelbstein, *Phys. Chem. Chem. Phys.* **2018**, *20*, 4092.

[30] K. Januszko, R. Chetty, T. Mashimo, K. Wojciechowski, *Mechanik* **2016**, 522.

[31] E. Hazan, O. Ben-Yehuda, N. Madar, Y. Gelbstein, *Adv. Energy Mater.* **2015**, *5*, 1500272.

[32] E. M. J. Hedegaard, S. Johnsen, L. Bjerg, K. A. Borup, B. B. Iversen, *Chem. Mater.* **2014**, *26*, 4992.

[33] Y. Noda, M. Orihashi, H. Kaibe, Y. Imai, I. Shiota, I. A. Nishida, *15th Int. Conf. Thermoelectr.* **1996**, 146.

[34] Y. Gelbstein, Z. Dashevsky, M. P. Dariel, *Phys. B Condens. Matter* **2007**, *391*, 256.

[35] I. Bharti, N. Gupta, K. M. Gupta, *Int. J. Mater. Mech. Manuf.* **2013**, *1*, 221.

[36] Z. Dashevsky, Y. Gelbstein, I. Edry, I. Drabkin, M. P. Dariel, *22th Int. Conf. Thermoelectr.* **2003**, 421.

[37] J. L. Cui, X. B. Zhao, *Mater. Lett.* **2003**, *57*, 2466.

[38] Z. Dashevsky, M. P. Dariel, S. Shusterman, *Quantum Electron.* **2000**, 181.

[39] E. M. J. Hedegaard, A. A. H. Mamakhel, H. Reardon, B. B. Iversen, *Chem. Mater.* **2018**, *30*, 280.

[40] C. L. Cramer, J. Gonzalez-Julian, P. S. Colasuonno, T. B. Holland, *J. Eur. Ceram. Soc.* **2017**, *37*, 4693.

[41] J. Schilz, L. Helmers, W. E. Müller, M. Niino, *J. Appl. Phys.* **1998**, *83*, 1150.

[42] H. Li, H. Jing, Y. Han, G. Q. Lu, L. Xu, T. Liu, *J. Alloys Compd.* **2016**, *659*, 95.

[43] T. Itoh, T. Muto, K. Kitagawa, *2006 Int. Conf. Thermoelectr.* **2006**, 623.

[44] Y. S. Kang, M. Niino, I. A. Nishida, J. Yoshino, *17th Int. Conf. Thermoelectr.* **1998**, 429.

[45] H. Kaibe, I. Aoyama, M. Mukoujima, T. Kanda, S. Fujimoto, T. Kurosawa, H. Ishimabushi, K. Ishida, L. Rauscher, Y. Hata, S. Sano, *2005 Int. Conf. Thermoelectr.* **2005**, 227.

[46] Y. S. Kang, S. Moriya, K. Kisara, M. Niino, Y. Noda, L. Chen, T. Sudo, *16th Int. Conf. Thermoelectr.* **1997**, 390.

[47] T. Muto, K. Tokuda, T. Itoh, K. Kitagawa, *2005 Int. Conf. Thermoelectr.* **2005**, *2005*, 524.

[48] J. Schilz, L. Helmers, Y. S. Kang, Y. Noda, M. Niino, *16th Int. Conf. Thermoelectr.* **1997**, 375.

[49] M. S. El-genk, H. H. Saber, *Energy Convers. Manag.* **2003**, *44*, 1069.

[50] T. T. Wallace, Z.-H. Jin, J. Su, *J. Electron. Mater.* **2016**, *45*, 2142.

[51] W. Glatz, E. Schwyter, L. Durrer, C. Hierold, *J. Microelectromechanical Syst.* **2009**, *18*, 763.

[52] M. Smith, Y. S. Choi, C. Boughey, S. Kar-narayan, *Flex. Print. Electron.* **2017**, *2*, 015004.

[53] N. W. Ashcroft, N. D. Mermin, *Solid State Physics*; Harcourt, 1976.

[54] C. J. Yao, H. L. Zhang, Q. Zhang, *Polymers (Basel).* **2019**, *11*, 1.

[55] J. C. Maxwell, *A Treatise on Electricity and Magnetism*; 3rd ed.; Oxford University Press, 1904.

[56] R. B. Bird, W. E. Stewart, E. N. Lightfoot, *Transport Phenomena*; 2nd ed.; John Wiley & Sons, 2007.

[57] K. Pietrak, T. S. Wisniewski, *J. Power Technol.* **2015**, *95*, 14.